



**HAL**  
open science

# Deciphering the Interplay Between Local and Global Dynamics of Anodic Metal Oxidation

Aleksei Makogon, Jean-Marc Noël, Frédéric Kanoufi, Viacheslav Shkirskiy

► **To cite this version:**

Aleksei Makogon, Jean-Marc Noël, Frédéric Kanoufi, Viacheslav Shkirskiy. Deciphering the Interplay Between Local and Global Dynamics of Anodic Metal Oxidation. 2023. hal-04236078

**HAL Id: hal-04236078**

**<https://hal.science/hal-04236078v1>**

Preprint submitted on 10 Oct 2023

**HAL** is a multi-disciplinary open access archive for the deposit and dissemination of scientific research documents, whether they are published or not. The documents may come from teaching and research institutions in France or abroad, or from public or private research centers.

L'archive ouverte pluridisciplinaire **HAL**, est destinée au dépôt et à la diffusion de documents scientifiques de niveau recherche, publiés ou non, émanant des établissements d'enseignement et de recherche français ou étrangers, des laboratoires publics ou privés.

# Deciphering the Interplay between Local and Global Dynamics of Anodic Metal Oxidation

Aleksei Makogon, Jean-Marc Noël, Frédéric Kanoufi, Viacheslav Shkirskiy\*

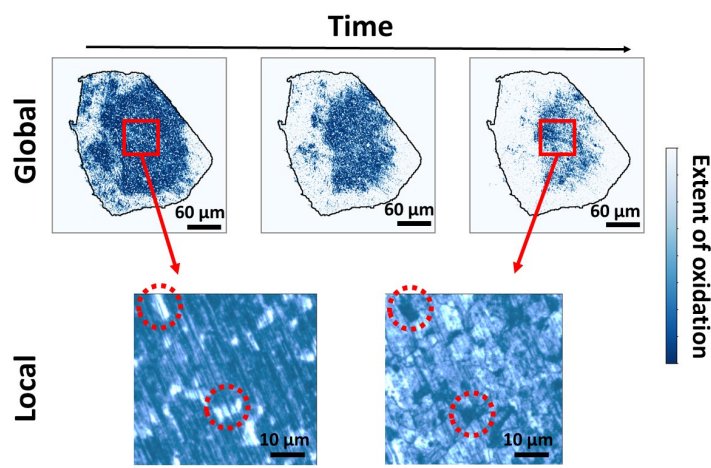
*Université Paris Cité, ITODYS, CNRS, 75013 Paris, France*

## Abstract

The stark difference between global and local metal oxidation dynamics underscores the need for methodologies capable of performing precise sub- $\mu\text{m}$ -scale and wide-field measurements. In this study, we present Reflective Microscopy (RM) as a tool developed to address this challenge, illustrated by the example of chronoamperometric Fe oxidation in NaCl solution. Analysis at a local scale of 10s of  $\mu\text{m}$  has revealed three distinct periods of Fe oxidation: the initial covering of the metal interface with a surface film, followed by the electrochemical conversion of the formed surface film, and finally, the in-depth oxidation of Fe. In addition, thermodynamic calculations and the quantitative analysis of changes in optical signal (light intensity), correlated with variations in refractive indexes, suggests the initial formation of hematite, followed by its subsequent conversion to magnetite. The reactivity maps for all three periods are heterogeneous, which can be attributed to the preferential oxidation of certain crystallographic grains. Notably, at the global scale of 100s of  $\mu\text{m}$ , reactivity initiates at the electrode border and progresses towards its center, demonstrating a unique pattern that is independent of local metal structure. This finding underscores the significance of simultaneously employing sub- $\mu\text{m}$ -precise and wide-field measurements for a comprehensive description of metal oxidation processes.

**Keywords:** Optical Microscopy, Metal Oxidation, Film Growth, Global vs Local Dynamics, Iron

**Corresponding author:** [viacheslav.shkirskiy@cnrs.fr](mailto:viacheslav.shkirskiy@cnrs.fr)



## 1. Introduction

Recent advancements in the development and application of local probe techniques have highlighted the pronounced heterogeneity in metal oxidation, an attribute that is discernible even within pure metal phases.<sup>1-5</sup> The isolation of individual grains and grain boundaries within a nanodroplet electrochemical cell - also known as Scanning Electrochemical Cell Microscopy (SECCM) - demonstrated that these grain boundaries exhibit the most substantial electrochemical activity within a polycrystalline metal structure.<sup>6-11</sup> The rate of oxidation was shown to be linked with the increase in grain boundary energy, the density of fractured bonds at the grain boundary plane, and the energy of metal oxidation on individual facets.<sup>6,7,12,13</sup> This discovery presents a significant challenge to conventional methods of interpreting global electrochemical measurements, which have often been premised on the assumption of uniform metal reactivity.<sup>14-17</sup> Simultaneously, it is important to note that global reactivity cannot be solely inferred from the measurements of isolated nanoscopic areas. This is due to the cooperative interplay between metal heterogeneities resulting from the formation of extensive galvanic couplings,<sup>18,19</sup> the diffusive exchange of dissolved species,<sup>20-23</sup> among other factors.<sup>24</sup> As a result, conducting a comprehensive analysis of metal oxidation reactions necessitates the formulation and implementation of methodologies—ones that balance both highly precise measurements, capable of delving into nanometer-scale intricacies, and wide-field measurements that can cover expanses up to the millimeter range.<sup>25</sup> This dual-pronged approach would effectively capture the nuanced interplay between the local and global dynamics intrinsic to metal oxidation, thereby providing a robust, holistic understanding of the process. To tackle this challenge and demonstrate the merits of dual-pronged, precision-focused and wide-field, in-situ measurements in the realm of metal oxidation, we utilized Reflective Microscopy (RM).

RM is a label-free optical imaging technique that leverages local changes in the refractive index at the image interface to elucidate various (electro-)chemical phase transformations.<sup>26-34</sup> It is particularly valuable in corrosion research as changes in optical intensities can be quantitatively linked to both the thickness (down to nanometer levels) and composition of surface films.<sup>23,25,26</sup> These parameters are central to our understanding of metal passivation and corrosion protection. When augmented with machine vision methodologies,<sup>35,36</sup> RM evolves into an automated, robust, and flexible approach. Its versatility and efficacy are further demonstrated in this work through the examination of corrosion in pure polycrystalline Fe metal in NaCl medium.

With a primary focus on illustrating the methodological approach of combined global and local observations, we selected Fe as our subject, given its status as one of the most extensively studied systems in the field of corrosion. The distinctive aspect of our research lies in conducting localized opto-electrochemical measurements observing the entire metal interface at the millimeter scale with sub- $\mu\text{m}$  precision during the global application of chronoamperometric Fe oxidation. In doing so, we can correlate both global electrochemical and an assembly of local optical data, providing unique

insight into the interplay between local and global metal oxidations. Moreover, we have developed and publicly shared an automated data processing procedure that reproduces all images and substantiates all the conclusions drawn in this manuscript. Overall, this study underscores the significance of adopting a dual-pronged strategy in electrochemical research, one that combines precision-focused and wide-field, in-situ approaches.

## 2. Experimental

### 2.1. Materials

A rod of > 98% pure Fe, with a diameter of 9.5 mm and a length of 50 cm, was sourced from GoodFellow. This rod was manually sharpened and cut to form an approximate 1 cm cone. The resulting cone was then embedded in a quick-set epoxy adhesive (RS PRO 850-940), allowed to air-dry, and then polished using 320-grit SiC until the Fe surface at the tip of the cone was exposed with the surface area of 0.0015 cm<sup>2</sup>. Immediately prior to experimentation, the sample was successively polished using 400, 600, and 1200 grit SiC under tap water cooling. The sample was subsequently cleaned with ethanol and deionized water, gently air-dried, and then placed in the electrochemical cell. All experiments were conducted in aqueous solutions of 5 mM NaCl (analytical grade, VWR Prolabo), prepared using water purified by a Millipore™ system (18 MΩ×cm).

### 2.2. Reflective microscopy (RM) methodology

#### 2.2.1. Measurement principle

The Fe sample, embedded in epoxy and polished, was fixed at the bottom of a homemade cylindrical cell. This setup exposed a circular area of approximately 50 mm<sup>2</sup>. Of this area, only 0.0015 cm<sup>2</sup> was the Fe surface, while the remaining area consisted of the epoxy resin. The cell was then placed into a Reflective Microscopy (RM) setup, with light illumination and collection occurring from the top (Fig. 1a). The Fe electrode was connected as the working electrode at the base of the cell, while the Pt counter and 3.4 M Ag/AgCl reference electrodes were also positioned at the bottom, controlled by a CHI 660A Potentiostat. Further details of the in-house developed RM setup can be found elsewhere.<sup>23,29</sup> Briefly, the setup included an Olympus microscope equipped with a water immersion objective (magnification ×10, 1.00-NA, Olympus LUMPlanFLN W) having a focal distance of approximately 3.5 mm, and an SVCam exo541MU3 CCD camera (SVS-Vistek GmbH, 4496×4504 pixels, 12 bit) operating at 10-25VDC. In this work, we employed binning to reduce the resolution by a factor of 2 in both x and y dimensions, thereby increasing the acquisition rate of the camera. Therefore, the size of each individual pixel was approximately 0.5 μm. A halogen white lamp, filtered at λ = 490 nm blue light using an interference filter (spectral bandwidth of 20 nm), served as the light source. The substrate was top-illuminated by the blue light beam via the microscope objective. The same objective collected the reflected light, directing it to the CCD camera, thus enabling real-time imaging of the light flux reflected by the analyzed surface. Prior to the experiment, we ensured the

planarity of the analyzed surface area (with a precision of  $10^{-2}$  degrees) using an interference Mirau objective (magnification  $\times 10$  (CF Plan, Nikon)) by minimizing the number of interference fringes over the imaged plane. Next, we gently poured 20 mL of 5 mM NaCl solution into the cell. After making focus adjustments in the optical microscope and measuring the open circuit potential (OCP) for about 5 minutes, we initiated chronoamperometry at a potential of +0.1 V vs OCP. Simultaneously, image acquisition began at a rate of 10 Hz. After 3-6 minutes, we halted the image acquisition and potential application, then removed and repolished the substrate. To ensure the statistical significance of our observations, we repeated the experiment a total of four times.

### 2.2.2. Data processing

The central concept underpinning our data processing is that the light reflectivity ( $R$ ) is proportional to both the thickness ( $\delta$ ) and the composition (via its refractive index  $n$ ) of surface films on metal substrates.<sup>23,29,31,36,37</sup> This principle, rooted in the notion of light interference reflected from the metal interface and surface films (Fig. 1a), has already been substantiated for flat Fe<sup>29</sup> and Al-based substrates.<sup>23,36</sup> It is derived from the Fresnel equations, the specifics of which can be found in another sources.<sup>23,29,31,37</sup> Among all phases of Fe oxides reported during Fe oxidation, we considered the most thermodynamically stable phases, Fe<sub>3</sub>O<sub>4</sub> and Fe<sub>2</sub>O<sub>3</sub> (Fig. 2b),<sup>38-41</sup> also known respectively as magnetite and hematite. Further discussion on this topic can be found later in the manuscript. Theoretical variations of reflectivity intensities ( $1 + \Delta R/R$ ) have been plotted in Fig. 2a. The input values for simulations are as follows (for  $\lambda = 490$  nm):  $n_{Fe} = 1.06 + 4.99i$ ,  $n_{Fe_3O_4} = 2.42$ ,  $n_{Fe_2O_3} = 2.92$ ,  $n_{H_2O} = 1.3$ .<sup>42-45</sup> To compare the theoretical predictions with experimental values, the intensity of the reflected light ( $I(t)$ ) has been normalized by the light intensity at  $t=0$ :

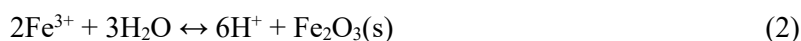
$$\frac{I(t)}{I(t=0)} = 1 + \frac{\Delta R}{R} \quad (1),$$

where  $t$  stands for time. Please note that the Fresnel approximation is primarily used for relative comparisons between surface films of different chemical compositions and the study of relative film distribution, as the absolute estimation of surface films can be confounded by the roughness of the as-prepared Fe surface. All data processing was executed in a Jupyter Lab environment powered by Python 3. The original data and Python code that produced all images in this manuscript are available in the Zenodo repository (<https://doi.org/10.5281/zenodo.8341764>) under the terms of a Creative Commons Attribution 4.0 International license.

### 2.3. Computation of chemical equilibrium diagram

A potential-pH diagram for Fe was generated using the HYDRO Medusa Chemical Equilibrium Software to elucidate the observed Fe oxidation behavior.<sup>38</sup> The software-provided potential versus standard hydrogen electrode (SHE) was recalibrated, considering that the potential of a 3.4 M Ag/AgCl solution is -0.2 V relative to SHE.<sup>46</sup> The soluble Fe species considered in the study were

Fe<sup>2+</sup>, Fe(OH)<sub>2</sub><sup>+</sup>, Fe(OH)<sub>3</sub>, Fe(OH)<sub>4</sub><sup>-</sup>, Fe<sub>2</sub>(OH)<sub>2</sub><sup>4+</sup>, Fe<sub>3</sub>(OH)<sub>4</sub><sup>5+</sup>, FeO<sub>4</sub><sup>2-</sup>, FeOH<sup>2+</sup>, Fe(OH)<sub>2</sub>, Fe(OH)<sub>3</sub><sup>-</sup>, Fe(OH)<sub>4</sub><sup>2-</sup>, FeOH<sup>+</sup>, FeCl<sub>2</sub><sup>+</sup>, FeCl<sub>2</sub><sup>-</sup>, FeCl<sub>3</sub>, FeCl<sub>4</sub><sup>-</sup> and FeCl<sup>+</sup>. In addition, the solid Fe species taken into account were Fe(OH)<sub>3</sub>(s), Fe<sub>2</sub>O<sub>3</sub>(s), FeOOH(s), Fe(OH)<sub>2</sub>(s), Fe<sub>3</sub>(OH)<sub>8</sub>(s), and Fe<sub>3</sub>O<sub>4</sub>(s) and Fe(OH)<sub>2.7</sub>Cl<sub>0.3</sub>(s). The calculation was conducted at a temperature of 25 °C, with the total concentration of Fe species held at 0.1 M, and a NaCl concentration of 5 mM. All equilibrium constants for the given species were used as reported in the software database,<sup>38,47</sup> except for Fe<sub>2</sub>O<sub>3</sub> (hematite) and Fe(OH)<sub>2.7</sub>Cl<sub>0.3</sub>(s). For hematite, we adjusted the equilibrium constant (*K*) to account for a deviation in the reported values of its Gibbs free energy of formation,<sup>39,47,48</sup> thereby ensuring a better correlation with the results reported in our study. We set the lg*K* of the reaction



to -1.5, in accordance with the notation used in the Hydro Meduza Database entries.<sup>38</sup> We also adjusted the *K* value for Fe(OH)<sub>2.7</sub>Cl<sub>0.3</sub>(s) formation from 3.0 (as reported in the Hydro Meduza database) to 1.0 (as used in this study), significantly suppressing its formation. This is consistent with literature reports indicating suppression of Cl-containing Fe corrosion products at the low Cl concentrations we utilized.<sup>49</sup>

### 3. Results and Discussion

#### 3.1. Chronoamperometric Analysis of Fe Oxidation: The Three Periods

We coupled a conventional three-electrode electrochemical setup with in-situ RM observations to aid in interpreting the global electrochemical current during potentiostatic Fe oxidation (Fig. 1a). Before Fe oxidation, the Fe electrode was polished with 1200 grit SiC, thereby creating a surface roughness of 5 μm. This process rendered visible, optically discernable directional polishing lines, as illustrated in Fig. 1b. This procedure was carried out deliberately to investigate any possible correlation between the direction of the polishing lines and the propagation pattern of corrosion. To ensure complete visibility under an optical microscope (Fig. 1b), the Fe electrode was designed with a surface area of 0.0015 cm<sup>2</sup>, comparable to standard sizes in macroscale electroanalytical analysis. This setup facilitated direct correlation between the measured electrical current and the averaged optical reflectivity. The sample was then positioned in a corrosive electrolyte of 5 mM NaCl (neutral pH) within the opto-electrochemical setup. The OCP was measured for 5 minutes, yielding a value of -0.4 V vs 3M Ag/AgCl. During this period, no variations in the optical intensity were observed. An anodic potential of +0.1 V vs OCP was then applied for approximately 3 minutes. During this period, we recorded two independent measurements: the global electrochemical current from the potentiostat and the dynamic optical images of the Fe surface. The latter was achieved through a ×10 water immersion objective under illumination with blue light (490 nm) collected onto a CCD camera. Both electrochemical and optical measurements were recorded at an identical acquisition rate of 10 Hz. This experiment was

repeated 4 times in total (with the whole dataset available in the [Zenodo repository](#)), yielding identical trends that we analyzed in detail based on a typical example discussed below.

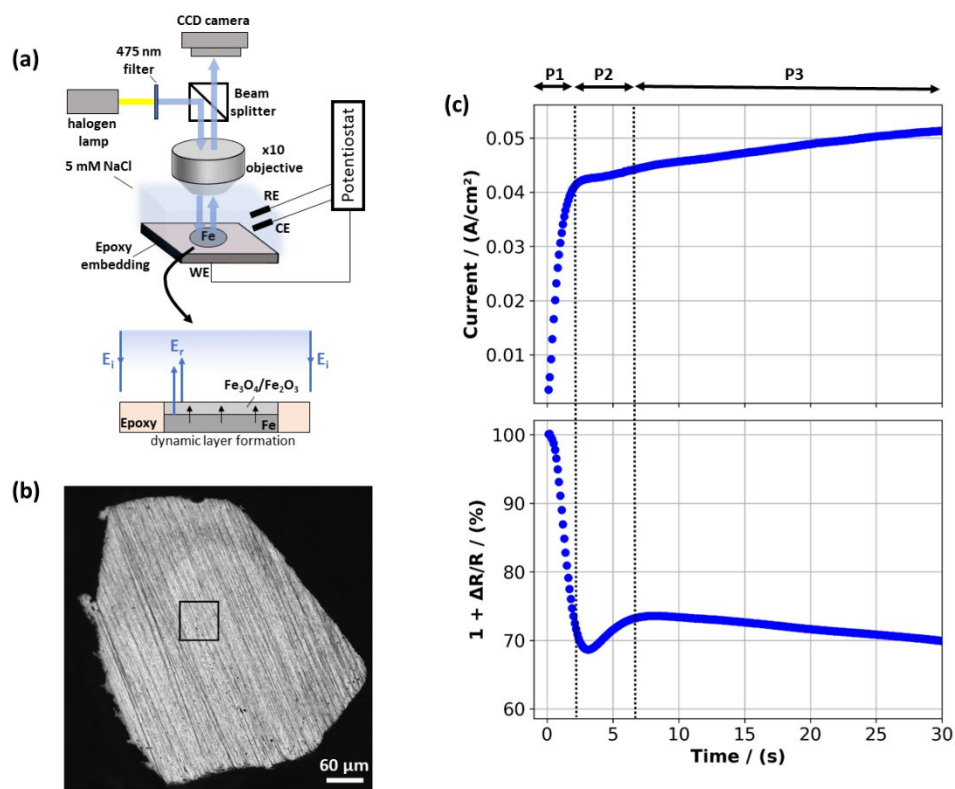
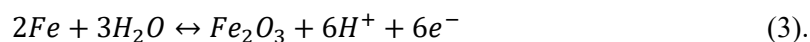


**Fig. 1** (a) Schematic illustration of the RM approach, coupled with electrochemical characterization of a millimeter-sized Fe electrode. The top part of the figure provides a general view of the apparatus, while the bottom part illustrates the optical signal generation. Incident light ( $E_i$ ), filtered at 475 nm, is focused on the metal interface during potentiostatic oxidation. The collected light includes contributions from the reflected light ( $E_r$ ) from the surfaces of Fe oxides and the metal, which is proportional to the thickness of surface films and their chemical composition. (b) Optical image of the polished Fe interface, the back square corresponding to the surface optically monitored in Fig. 2c. (c) Plots of electrochemical current (top) and averaged normalized reflectivity (bottom) as a function of time during potentiostatic metal oxidation performed at  $-0.3$  V vs.  $3.4$  M KCl Ag/AgCl (or  $+0.1$  V vs. the OCP value) in a  $5$  mM NaCl solution. Dotted lines highlight the three distinct periods (P1, P2, and P3) observable from both the electrochemical and optical data. This experiment was repeated 4 times in total.

First, we examine the global electrical current and averaged optical signal, expressed as the evolution of averaged normalized intensity (Fig. 1c). Both curves reveal three distinct periods.

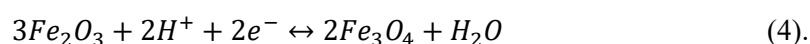
Period 1 (P1) initiates immediately upon potential imposition and lasts approximately 2-3 s. This period is characterized by a sudden current density increase up to  $0.04$  A/cm<sup>2</sup>, coupled with an abrupt decrease in surface reflectivity, by approximately 30%. These observations indicate surface-controlled

oxidation, leading to the formation of surface films. Based on the potential-pH diagram (Fig. 2b), this can be interpreted as the conversion of Fe to a hematite layer (denoted as  $\text{Fe}_2\text{O}_3$ ) at neutral pH, with a concurrent acidification of the environment due to water hydrolysis:



Upon analyzing raw optical images captured on a scale of 10s of  $\mu\text{m}$ , as demonstrated in Fig. 2c, a distinct heterogeneous darkening pattern emerges at the metal interfaces within the 0-s to 2-s timeframe. This pattern corresponds to the localized extent of surface oxidation. Intriguingly, the direction of polishing seems to exert minimal influence on this pattern's distribution. Areas exhibiting a polygonal shape and sizes smaller than 10  $\mu\text{m}$  (circled for emphasis) notably sustain a lighter hue, which closely resembles the metal crystallographic texture.<sup>6-11</sup> It is crucial to mention that our experiment utilized pure Fe, effectively eliminating chemical heterogeneities as a potential explanation for the observed patterning.

Period 2 (P2) follows immediately and lasts about 5 seconds. It is discernable by a slight decrease in current density (Fig. 1c, top graph, P2) and a marked increase in normalized reflectivity, from approximately 70 % to about 75 % (Fig. 1c, bottom graph, P2). An assessment of localized raw optical images at the 7-s mark, as depicted in Fig. 2c, reveals a notable contrast shift. Areas that appeared bright in the 2-s image have since darkened, while areas that were initially dark have become noticeably brighter. A modest reduction in current density at this point could be indicative of cathodic (reduction) processes. Examining the potential vs pH diagram in Fig. 2b suggests that a shift in local pH, as a result of Eq. 3, might prompt the reduction from the hematite Fe(III) phase to the mixed Fe(II)/Fe(III) magnetite phase at a set potential of -0.3 V (highlighted by an arrow in Fig. 2b), consistent with the conditions of our experiment:



The simulated optical response in Fig. 2a concurs with this explanation. Given the similar densities of hematite and magnetite ( $\rho_{\text{Fe}_2\text{O}_3} = 5.2 \text{ g/cm}^3$  and  $\rho_{\text{Fe}_3\text{O}_4} = 5.0 \text{ g/cm}^3$ ), their interconversion would not yield a substantial alteration in the thickness of the surface layer. At the same time, for identical thickness of surface films, the hematite layer absorbs more light than the magnetite layer, therefore causing the reflectivity to increase during the described surface layer transformation (indicated with the dashed arrow in Fig. 2a).



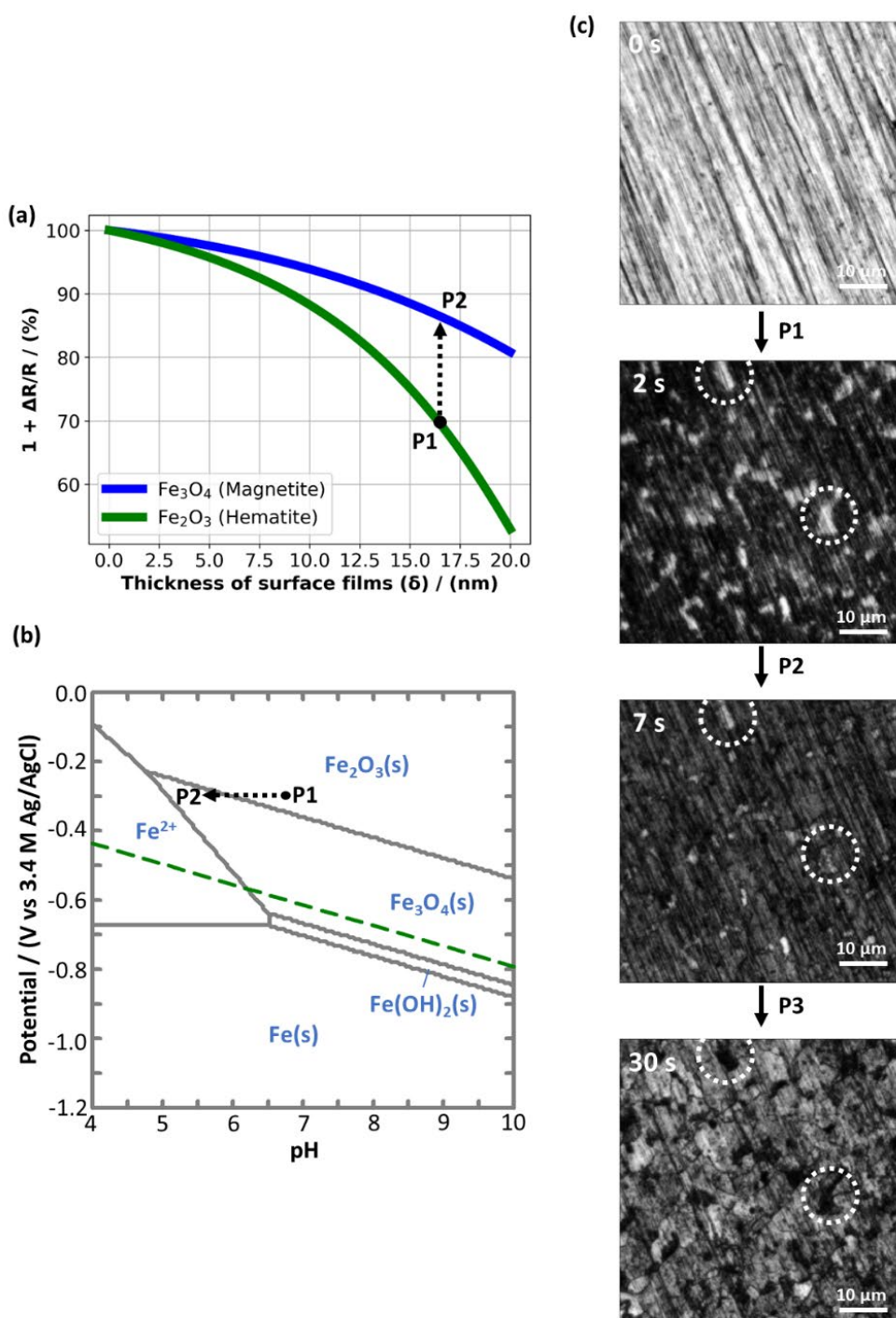


**Fig. 2** (a) Evolution of normalized reflectivity as a function of surface film thickness for magnetite and hematite, estimated using the Fresnel equation. (b) A potential-pH diagram for Fe, calculated using the HYDRO Medusa Chemical Equilibrium Software<sup>38</sup> with details reported in experimental section. The green dotted line represents proton reduction. The dotted arrow in both (a) and (b) illustrates the proposed transition between Periods 1 (P1) and 2 (P2) observed in the chronoamperometric experiment. (c) Optical images of the Fe surface (see inset in Fig. 1b) taken at 0, 2, 7, and 30 seconds into the chronoamperometric process, showcasing the transition between P1, P2, and P3. The white dotted circles are depicted over identical locations to serve as visual references.

Period 3 commences around the 7-second mark, extending until the culmination of the polarization experiment. This phase exhibits a consistent increase in current, as seen in Fig. 1c. Local optical image, captured at the 30-second interval and presented in Fig. 2c, demonstrates a marked darkening of the initially bright sections on the Fe surface. These sections were first observed in the 2- and 7-second snapshots (indicated by white circles for easy reference). Contrarily, the areas that were dark in the 2- and 7-second images exhibit increased reflectivity. This phenomenon, as discussed earlier, could potentially result from the transformation of the initially formed hematite layer into magnetite on the surface. Interestingly, the reflectivity enhancement covers a much larger area than the localized surface darkening. However, despite the broadened region of increased brightness, the total reflectivity diminishes (Fig. 1c, bottom graph). This observation emphasizes that, in terms of absolute values, the darkening effect is dominant. Its confined distribution suggests a highly localized metal oxidation, which could be indicative of pits.

We wish to emphasize that, although the current reached significant values (ca. 0.05 A/cm<sup>2</sup>) by the end of the experiment, the total charge consumed was only around 1.3 C/cm<sup>2</sup>, given the brief duration (30 s) of the chronoamperometric test. This translates, on average, to the formation of surface films of about 300 nm (detailed in Eq. 5). Considering the density difference between Fe ( $\rho_{Fe}=7.8$  g/cm<sup>3</sup>) and Fe oxides (assumed as  $\rho_{Fe_2O_3} = 5.2$  g/cm<sup>3</sup>), the height of the interface should increase by approximately 150 nm at the end of the experiment. With the high x10 magnification of our objective lens, such a minor shift in focus distance should not impact our optical measurements, which would need to be in the  $\mu$ m range to be noticeable.

In the subsequent sections, we will describe the spatial distribution of reflectivity alterations for the entirety of oxidized Fe interface and establish a quantitative correlation between current and optical intensities. This approach will furnish localized insights into the transformations of surface films and provide further justification of the proposed mechanistic sequence.

### 3.2. Period 1: Initial Formation of Surface Films on Fe Interface

Fig. 3a illustrates the spatial distribution of normalized optical intensities across the entire surface of the Fe electrode during the initial stages of chronoamperometry, reflecting the propagation of surface film formation. To improve contrast and enhance visual representation, light intensities of frame ( $N$ ) were normalized by frame ( $N-10$ ), as indicated by the subscript  $\Delta R_{10}$  throughout the manuscript. This normalization method is particularly useful for highlighting subtle differences in a series of images and is consistently applied to all image series below.

Upon examining the images of the entire Fe interface at 0.8 s, 1.0 s, and 1.5 s in Fig. 3a, it is apparent that the darkening of the metal interface starts preferentially at the edge of the Fe electrode and then propagates towards the center of the electrode. It is important to note that the initial image at 0 s (not displayed here but available in the [Zenodo repository](#)) exhibits a completely white appearance. This

corresponds to 100% of  $1+\Delta R_{10}/R$ , indicating that there were no observable changes prior to the application of chronoamperometry, which commenced at the 0-second mark. The areas outside of the electrode are filled with an epoxy resin where no changes occur, hence the normalized reflectivity remains at 100%, as indicated by the white color in the chosen color scheme of Fig. 3a. The surface darkening towards the electrode center is not discernible on the 10  $\mu\text{m}$  scale from the image insets in Fig. 2c and is only noticeable due to the observation of the entire active area at the scale of hundreds of  $\mu\text{m}$ . This observation suggests that the kinetics of localized oxidation are significantly influenced by the electrode's border at the mm scale, apart from the influence of the Fe interface's crystallographic structure at the  $\mu\text{m}$  scale.

Assuming that the reflectivity change obeys the Fresnel law – that is, it is directly related to the formation of surface films – the first derivative of the averaged reflectivity change should be proportional to the current density. We considered only data from the initial 2 seconds, during which the surface films were presumed to be predominantly composed of hematite, as discussed in the previous section. As shown in Fig. 3b, the current density and optical reflectivity - both independent measurements - indeed share a relationship during the initial period of oxidation. Subsequently, we used current density values to recalculate the average thickness of hematite surface films as function of time ( $\delta(t)$ ), assuming 100% Faradaic efficiency:

$$\delta(t) = \frac{Q(t)M_{\text{Fe}_2\text{O}_3}}{2nF\rho_{\text{Fe}_2\text{O}_3}} \quad (5),$$

where  $Q(t)$  is the cumulative charge normalized by the electrode surface area of 0.0015  $\text{cm}^2$ ,  $M_{\text{Fe}_2\text{O}_3}$  is the molar mass of hematite (160 g/mol),  $n$  is the number of electrons per consumed Fe metal ( $n=3$ ),  $F$  is the Faraday constant (96500 C/mol) and  $\rho_{\text{Fe}_2\text{O}_3}$  is the density of hematite layer (5.2  $\text{g}/\text{cm}^3$ ). Factor 2 was added to account the stoichiometry between Fe and  $\text{Fe}_2\text{O}_3$  in Eq. 3. The evolution of surface films thus calculated is plotted against the change in normalized reflectivity in Fig. 3c (dotted line). The solid line in Fig. 3c shows the theoretical optical response for a hematite layer, replicated from Fig. 2a.

Although there's a minor discrepancy between the two curves - with the solid curve displaying an arch-like shape while the dotted curve tends more towards linearity - their overall correlation is satisfactory. This minor divergence could arise due to the surface film already transitioning from hematite to magnetite, as slight surface brightening can be noticed on the peripheries of the 1.5 s image in Fig. 3a. Another possible source of this deviation could be attributed to the initial Fe surface not being flawlessly flat. Instead, it exhibits an approximate 5  $\mu\text{m}$  roughness, akin to the roughness of the applied polishing pad. As a result, the optical simulations, ideally meant for flat surfaces, might diverge from the measured data and the current density, since the geometric surface area was utilized for current density calculations. Despite these oversimplifications, the congruity between the two

independent electrochemical and optical measurements fortifies the credibility of the estimated chemical composition presented in the potential vs pH diagram in Fig. 2b.

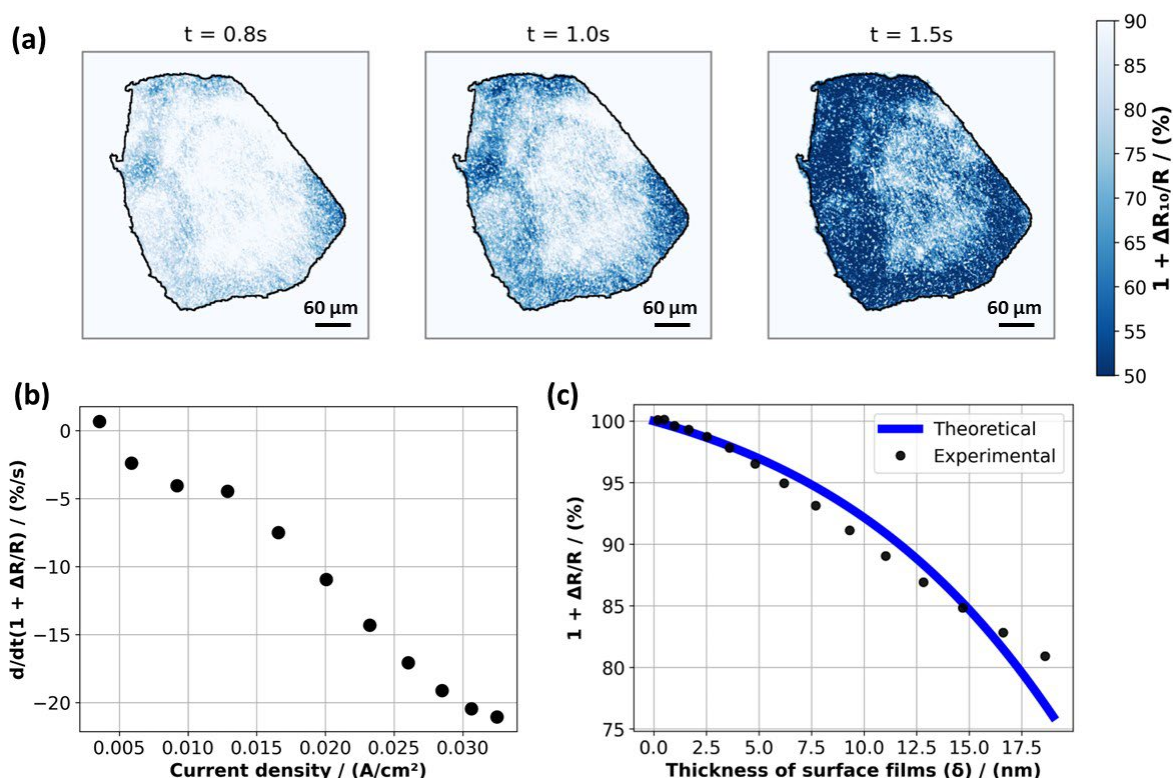


**Fig. 3** Analysis of Fe reactivity during P1. (a) Maps of normalized reflectivities after 0.8, 1.0, and 1.5 seconds of chronoamperometry. Reflectivity of frame ( $N$ ) is normalized by the reflectivity of frame ( $N-10$ ), as denoted in the subscript of the reflectivity change. The black line, which is placed for visual reference, underlies the area of the Fe electrode. (b) First derivative of averaged normalized reflectivity plotted as a function of electrochemical current density. (c) Experimental (black dots) and theoretical (blue line) change of normalized reflectivity with the increasing thickness of the hematite layer obtained from the values of the electrical current.

### 3.3. Period 2: Transformation and Evolution of Surface Films

During period 2, the surface brightens, as can be observed from Fig. 4, an effect associated with the transformation of hematite to magnetite in the surface layer. The normalized reflectivity starts to increase at the border of the Fe electrode in the image at 2.5 s, which rapidly propagates towards the center at 3.0 s and 3.5 s (Fig. 4). This transformation from hematite to magnetite is fundamentally electrochemical, but its rate should be strongly influenced by local pH as suggested by the potential vs pH diagram in Fig. 2b. In turn, the local pH should be dictated by the local oxidation rate of metallic Fe (Eq. 2). Consequently, despite its dependence on pH, the observed pattern of normalized reflectivity change - beginning at the border and gradually spreading towards the center of the

electrode - likely mirrors the gradient of electrochemical activity, similar to the variations in optical intensity witnessed during period 1.

Having demonstrated the adequacy of estimating the average surface film thickness in Eq. 5 in the preceding section, we can reframe it to estimate the average flux of  $H^+$  ( $J_{H^+}$ ). By factoring in the stoichiometry from Eq. 3, we can express  $J_{H^+}$  as follows:

$$J_{H^+} = i/F \quad (6),$$

where  $i$  represents the electrochemical current density. Applying the first Fick's law in a one-dimensional scenario,<sup>50</sup> the surface pH can be formulated under the steady-state assumption as:

$$pH_{surf} = -\lg \left( \frac{J_{H^+}}{D_{H^+}} x + C_{bulk} \right) \quad (7),$$

where  $D_{H^+}$  is the diffusion coefficient of  $H^+$  ( $9.3 \cdot 10^{-9} \text{ m}^2/\text{s}$ ),<sup>50</sup>  $x$  signifies the thickness of the diffusion layer (presumed to be 150 nm, a typical measure for a stagnant electrolyte under natural convection conditions),<sup>51,52</sup> and  $C_{bulk}$  represents the bulk concentration of  $H^+$  (considered as  $10^{-7} \text{ M}$ ). According to Eq. 7, the observed current increase from 0.001 to 0.04  $\text{A}/\text{cm}^2$  during the initial 0.1-2.5 s (during P1) of the experiment could result in a pH decrease to values between 5.7 and 4.2.

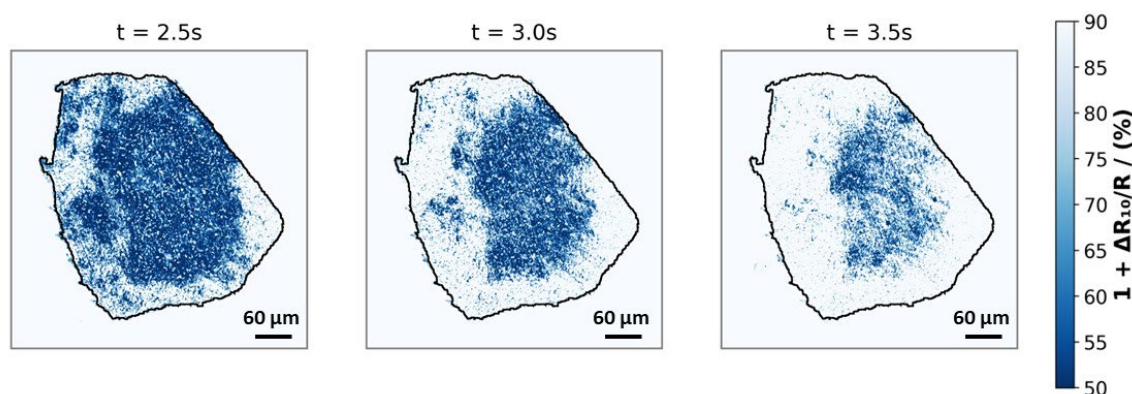


**Fig. 4** Analysis of Fe reactivity during P2. This figure displays maps of normalized reflectivities at 2.5, 3.0, and 3.5 seconds into the chronoamperometry. The reflectivity of each frame ( $N$ ) is normalized by the reflectivity of the preceding frame ( $N-10$ ), as indicated in the subscript of the reflectivity change. The black line, which is placed for visual reference, underlies the area of the Fe electrode.

The decline in pH to around 5 aligns with the proposed transition from P1 to P2, as illustrated in the potential-pH diagram in Fig. 2b. This also indicates that the proposed transition could potentially commence as early as 0.1 s into the chronoamperometry process. The lack of such immediate transition may suggest kinetic limitations inhibiting the film transformation. A further decline in pH to values below 5 could potentially instigate the subsequent shift into the  $Fe^{2+}$  region, thereby causing the dissolution of surface films. While the scenario seems thermodynamically feasible, the evident

darkening at the metal interface points towards negligible metal dissolution. This could denote a kinetic hindrance in the dissolution process and/or elevated local concentrations of Fe ions, which could foster the formation of surface films.

### 3.4. Period 3: Progressive In-Depth Metal Oxidation

Fig. 5a presents the spatial distribution of the evolution of normalized reflectivity during the last stage ( $t > 7$  s) of chronoamperometry application. In this period, the changes are more subtle, providing a milder contrast between different areas of the electrode. Consequently, the scale of the color scheme was adjusted with a reflectivity of 100%, representing the epoxy surface surrounding the Fe electrode, depicted in light blue color.

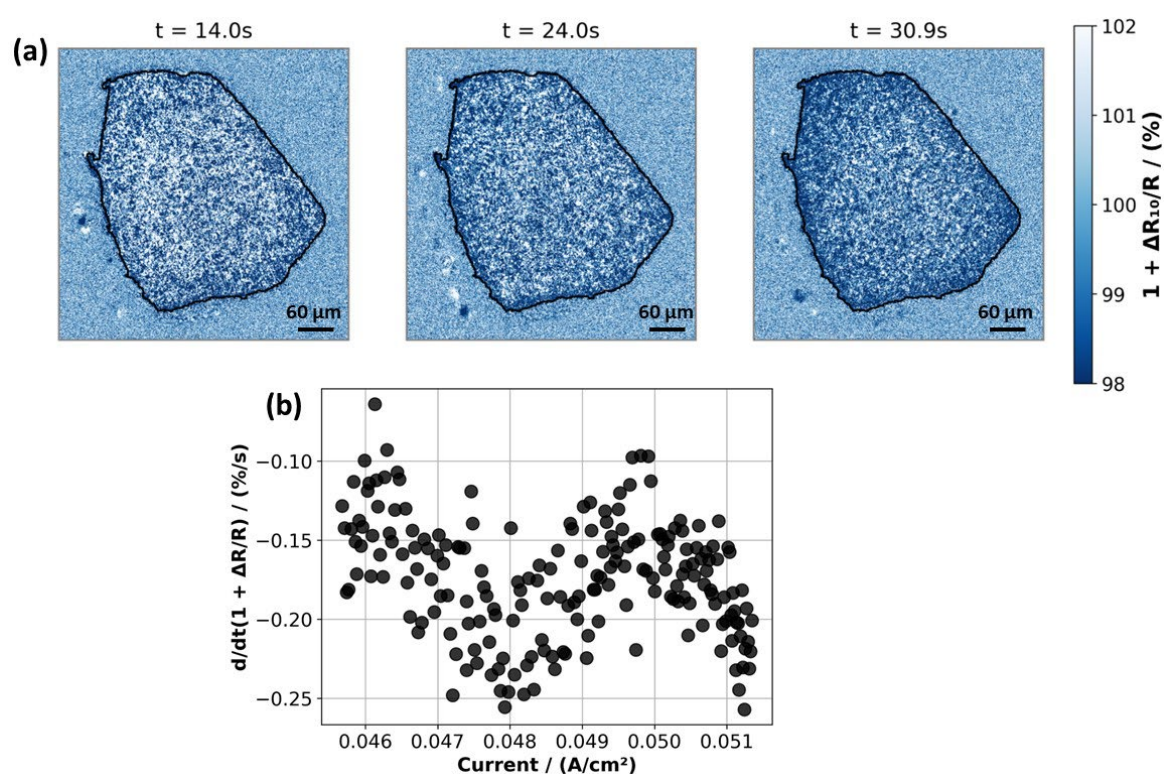


**Fig. 5.** Analysis of Fe reactivity during P3. (a) Maps of normalized reflectivities taken at 14.0, 24.0, and 30.9 seconds into the chronoamperometry process. The reflectivity of each frame ( $N$ ) is normalized by the reflectivity of the preceding frame ( $N-10$ ), as indicated in the subscript of the reflectivity change. The black line, which is placed for visual reference, underlies the area of the Fe electrode. (b) The first derivative of averaged normalized reflectivity is plotted as a function of the electrical current density.

The darkening of the Fe electrode becomes apparent in the images taken at 14.0 s, 24.0 s, and 30.9 s (Fig. 5a). Notably, we also observe macroscopically that the darkening tends to initiate preferentially at the edge of the Fe electrode, gradually advancing towards the electrode's center. As discussed earlier, the darkening of the Fe interface during this period indicates localized in-depth progression

that can exceed the penetration depth of light into the surface film (several hundreds nm).<sup>31</sup> In theory, no changes in visible light should be discernible. However, the subtle changes observed in this case could be attributed to the fact that on certain grains, in-depth corrosion does not surpass the light penetration depth, rendering optical detection still feasible.

The proportion of the current resulting from the oxidation of these grains should be marginal compared to the typically in-depth, pit-like corrosion.<sup>53</sup> Therefore, only a minor correlation should exist between the current density and changes in normalized reflectivity. This hypothesis is validated in Fig. 5b, where we plot the first derivative of the changes in averaged normalized reflectivity against the current density, similar to what was done for period 1. As anticipated, a minor correlation was detected, observable through periodic intensity fluctuations in the range of 0.15% s<sup>-1</sup> (as shown on the y-axis in Fig. 5b). However, this observed variation is characteristically noisy and could be confounded by the stability of the light source at these signal levels, thereby complicating the interpretation of data for quantitative analysis. In line with the above discussions, these perceived periodic variations may signify subtle transformations in the surface film and/or film dissolution due to localized pH acidification.

In summary, observations made on a larger scale of hundreds of  $\mu\text{m}$  enabled us to probe the electrochemical dynamics of reactivity that begins at the electrode border and advances towards the center. Intriguingly, the direction of macroscale metal oxidation remained unaffected by the directional polishing lines present on the Fe substrate after sample preparation. While it is anticipated that electrode reactivity begins at the edge because of its increased accessibility,<sup>54-57</sup> this detail is frequently omitted in discussions on local metal oxidation and in considerations of polycrystalline metal surface reactivity in macroscale electroanalysis.<sup>1-5,14-17</sup> Our study offers direct evidence that enhanced reactivity at the electrode edge substantially influences grain-dependent localized current densities and cannot be overlooked.

#### 4. Conclusions

We investigated the anodic oxidation of polycrystalline pure Fe metal in 5 mM NaCl using a dual-pronged, precision-focused, and wide-field opto-electrochemical RM approach. This was done to reveal the interplay between local (at the scale of a 10s  $\mu\text{m}$ ) and global (at the scale of a 100s  $\mu\text{m}$ ) oxidation dynamics. The global electrochemical data and the averaged normalized intensities of reflected light across the entire surface indicated three distinct periods. These periods, backed by a direct correlation between electrochemical and optical data and thermodynamics simulations, were attributed to: (i) the initial covering of the Fe interface with a hematite layer, (ii) the subsequent transformation of hematite to magnetite, and (iii) in-depth Fe oxidation. Across all three periods, at a local scale, the absolute magnitude of reactivity consistently followed a polygonal pattern approximately 10  $\mu\text{m}$  in size, a pattern that resembles the crystallographic structure of the metal.

Contrastingly, at a macroscopic level, the electrode's proximity to the edge dictates its kinetics and the degree of local oxidation. This research underscores the importance of considering both local and global dynamics in a comprehensive analysis of electroactive interfaces, offering a quantitative framework for optical signal analysis to address this challenge.

## 5. Acknowledgements

This work was partially financially supported by the Agence Nationale de la Recherche 10 (ANR) Jeunes chercheuses, jeunes chercheurs, ANR JCJC, program (OCTAWA project, ANR-11 22-CE29-0010-01).

## 6. References

- (1) Li, Y.; Morel, A.; Gallant, D.; Mauzeroll, J. Correlating Corrosion to Surface Grain Orientations of Polycrystalline Aluminum Alloy by Scanning Electrochemical Cell Microscopy. *ACS Appl. Mater. Interfaces* **2022**, *14* (41), 47230–47236. <https://doi.org/10.1021/acsami.2c12813>.
- (2) Bentley, C. L. Scanning Electrochemical Cell Microscopy for the Study of (Nano)Particle Electrochemistry: From the Sub-Particle to Ensemble Level. *Electrochem. Sci. Adv.* **2022**, *2* (3), e2100081. <https://doi.org/10.1002/ELSA.202100081>.
- (3) Daviddi, E.; Shkirskiy, V.; Kirkman, P. M.; Robin, M. P.; Bentley, C. L.; Unwin, P. R. Screening the Surface Structure-Dependent Action of a Benzotriazole Derivative on Copper Electrochemistry in a Triple-Phase Nanoscale Environment. *J. Phys. Chem. C* **2022**, *126* (35), 14897–14907. <https://doi.org/10.1021/acs.jpcc.2c04494>.
- (4) Daviddi, E.; Gaudin, L. F.; Bentley, C. L. Scanning Electrochemical Cell Microscopy: High-Resolution Structure–property Studies of Mono- and Polycrystalline Electrode Materials. *Curr. Opin. Electrochem.* **2022**, *34*, 101006. <https://doi.org/10.1016/j.coelec.2022.101006>.
- (5) Ryu, C. H.; Lee, H.; Lee, H.; Ren, H. Learning from the Heterogeneity at Electrochemical Interfaces. *J. Phys. Chem. Lett.* **2022**, *13* (33), 7838–7846. <https://doi.org/10.1021/ACS.JPCLETT.2C02009>/ASSET/IMAGES/MEDIUM/JZ2C02009\_0009.GIF.
- (6) Shkirskiy, V.; Yule, L. C.; Daviddi, E.; Bentley, C. L.; Aarons, J.; West, G.; Unwin, P. R. Nanoscale Scanning Electrochemical Cell Microscopy and Correlative Surface Structural Analysis to Map Anodic and Cathodic Reactions on Polycrystalline Zn in Acid Media. *J. Electrochem. Soc.* **2020**, *167* (4), 041507. <https://doi.org/10.1149/1945-7111/ab739d>.
- (7) Wang, Y.; Li, M.; Ren, H. Interfacial Structure and Energy Determine the Heterogeneity in the Electrochemical Metal Dissolution Activity at Grain Boundary. *Chem. Mater.* **2023**, *35* (11),



- 4243–4249. <https://doi.org/10.1021/acs.chemmater.3c00220>.
- (8) Yule, L. C.; Shkirskiy, V.; Aarons, J.; West, G.; Bentley, C. L.; Shollock, B. A.; Unwin, P. R. Nanoscale Active Sites for the Hydrogen Evolution Reaction on Low Carbon Steel. *J. Phys. Chem. C* **2019**, *123* (39), 24146–24155. <https://doi.org/10.1021/acs.jpcc.9b07216>.
- (9) Gaudin, L. F.; Kang, M.; Bentley, C. L. Facet-Dependent Electrocatalysis and Surface Electrochemical Processes on Polycrystalline Platinum. *Electrochim. Acta* **2023**, *450*, 142223. <https://doi.org/10.1016/J.ELECTACTA.2023.142223>.
- (10) Daviddi, E.; Shkirskiy, V.; Kirkman, P. M.; Robin, M. P.; Bentley, C. L.; Unwin, P. R. Nanoscale Electrochemistry in a Copper/Aqueous/Oil Three-Phase System: Surface Structure–Activity–Corrosion Potential Relationships. *Chem. Sci.* **2021**, *12* (8), 3055–3069. <https://doi.org/10.1039/D0SC06516A>.
- (11) Mariano, R. G.; McKelvey, K.; White, H. S.; Kanan, M. W. Selective Increase in CO<sub>2</sub> Electroreduction Activity at Grain-Boundary Surface Terminations. *Science (80-. )*. **2017**, *358* (6367), 1187–1192. <https://doi.org/10.1126/science.aao3691>.
- (12) Yule, L. C.; Shkirskiy, V.; Aarons, J.; West, G.; Shollock, B. A.; Bentley, C. L.; Unwin, P. R. Nanoscale Electrochemical Visualization of Grain-Dependent Anodic Iron Dissolution from Low Carbon Steel. *Electrochim. Acta* **2020**, *332*, 135267. <https://doi.org/10.1016/j.electacta.2019.135267>.
- (13) Badwe, N.; Chen, X.; Schreiber, D. K.; Olszta, M. J.; Overman, N. R.; Karasz, E. K.; Tse, A. Y.; Bruemmer, S. M.; Sieradzki, K. Decoupling the Role of Stress and Corrosion in the Intergranular Cracking of Noble-Metal Alloys. *Nat. Mater.* **2018**, *17* (10), 887–893. <https://doi.org/10.1038/s41563-018-0162-x>.
- (14) Bernal, M.; Torres, D.; Parapari, S. S.; Čeh, M.; Rožman, K. Ž.; Šturm, S.; Ustarroz, J. A Microscopic View on the Electrochemical Deposition and Dissolution of Au with Scanning Electrochemical Cell Microscopy – Part I. *Electrochim. Acta* **2023**, *445*, 142023. <https://doi.org/10.1016/j.electacta.2023.142023>.
- (15) Daviddi, E.; Chen, Z.; Beam Massani, B.; Lee, J.; Bentley, C. L.; Unwin, P. R.; Ratcliff, E. L. Nanoscale Visualization and Multiscale Electrochemical Analysis of Conductive Polymer Electrodes. *ACS Nano* **2019**, *13* (11), 13271–13284. <https://doi.org/10.1021/acsnano.9b06302>.
- (16) Li, X.; Binnemans, K. Oxidative Dissolution of Metals in Organic Solvents. *Chem. Rev.* **2021**, *121* (8), 4506–4530. <https://doi.org/10.1021/acs.chemrev.0c00917>.
- (17) Kang, S.; Cho, S.; Kang, Y. M. Getting to the Bottom of Transition Metal Dissolution. *Nat. Nanotechnol.* **2023**. <https://doi.org/10.1038/s41565-023-01396-1>.

- (18) Jakab, M. A.; Little, D. A.; Scully, J. R. Experimental and Modeling Studies of the Oxygen Reduction Reaction on AA2024-T3. *J. Electrochem. Soc.* **2005**, *152* (8), B311–B320. <https://doi.org/10.1149/1.1949047>.
- (19) Hayden, S. C.; Chisholm, C.; Eichmann, S. L.; Grudt, R.; Frankel, G. S.; Hanna, B.; Headrick, T.; Jungjohann, K. L. Genesis of Nanogalvanic Corrosion Revealed in Pearlitic Steel. *Nano Lett.* **2022**, *22*, 7087–7093. <https://doi.org/10.1021/acs.nanolett.2c02122>.
- (20) Zou, N.; Zhou, X.; Chen, G.; Andoy, N. M.; Jung, W.; Liu, G.; Chen, P. Cooperative Communication within and between Single Nanocatalysts. *Nat. Chem.* **2018**, *10* (6), 607–614. <https://doi.org/10.1038/s41557-018-0022-y>.
- (21) Hughes, A. E.; Boag, A.; Glenn, A. M.; McCulloch, D.; Muster, T. H.; Ryan, C.; Luo, C.; Zhou, X.; Thompson, G. E. Corrosion of AA2024-T3 Part II: Co-Operative Corrosion. *Corros. Sci.* **2011**, *53* (1), 27–39. <https://doi.org/10.1016/j.corsci.2010.09.030>.
- (22) Denissen, P. J.; Homborg, A. M.; Garcia, S. J. Interpreting Electrochemical Noise and Monitoring Local Corrosion by Means of Highly Resolved Spatiotemporal Real-Time Optics. *J. Electrochem. Soc.* **2019**, *166* (11), C3275–C3283. <https://doi.org/10.1149/2.0341911jes>.
- (23) Godeffroy, L.; Makogon, A.; Derouich, S.; Kanoufi, F.; Shkirskiy, V. Imaging and Quantifying the Chemical Communication between Single Particles in Metal Alloy. *Anal. Chem.* **2023**, just accepted. <https://doi.org/10.1021/acs.analchem.3c01258>.
- (24) Tao, B.; McPherson, I. J.; Daviddi, E.; Bentley, C. L.; Unwin, P. R. Multiscale Electrochemistry of Lithium Manganese Oxide (LiMn<sub>2</sub>O<sub>4</sub>): From Single Particles to Ensembles and Degrees of Electrolyte Wetting. *ACS Sustain. Chem. Eng.* **2023**, *11* (4), 1459–1471. <https://doi.org/10.1021/acssuschemeng.2c06075>.
- (25) Shkirskiy, V.; Kanoufi, F. Reflective Microscopy for Mechanistic Insights in Corrosion Research. *Curr. Opin. Electrochem.* **2023**, *39*, 101259. <https://doi.org/10.1016/j.coelec.2023.101259>.
- (26) Pfaff, S.; Larsson, A.; Orlov, D.; Harlow, G. S.; Abbondanza, G.; Linpé, W.; Rämisch, L.; Gericke, S. M.; Zetterberg, J.; Lundgren, E. Operando Reflectance Microscopy on Polycrystalline Surfaces in Thermal Catalysis, Electrocatalysis, and Corrosion. *ACS Appl. Mater. Interfaces* **2021**, *13* (16), 19530–19540. <https://doi.org/10.1021/acsami.1c04961>.
- (27) Linpé, W.; Harlow, G. S.; Larsson, A.; Abbondanza, G.; Rämisch, L.; Pfaff, S.; Zetterberg, J.; Evertsson, J.; Lundgren, E. An Electrochemical Cell for 2-Dimensional Surface Optical Reflectance during Anodization and Cyclic Voltammetry. *Rev. Sci. Instrum.* **2020**, *91*, 044101. <https://doi.org/10.1063/1.5133905>.

- (28) Denissen, P. J.; Garcia, S. J. Reducing Subjectivity in EIS Interpretation of Corrosion and Corrosion Inhibition Processes by In-Situ Optical Analysis. *Electrochim. Acta* **2019**, *293*, 514–524. <https://doi.org/10.1016/j.electacta.2018.10.018>.
- (29) Chakri, S.; Patel, A. N.; Frateur, I.; Kanoufi, F.; Sutter, E. M. M.; Tran, T. T. M.; Tribollet, B.; Vivier, V. Imaging of a Thin Oxide Film Formation from the Combination of Surface Reflectivity and Electrochemical Methods. *Anal. Chem.* **2017**, *89* (10), 5303–5310. <https://doi.org/10.1021/acs.analchem.6b04921>.
- (30) Wint, N.; Ansell, P.; Edy, J.; Williams, G.; McMurray, H. N. A Method for Quantifying the Synergistic Inhibitory Effect of Corrosion Inhibitors When Used in Combination: A ‘Chromate Generating Coating.’ *J. Electrochem. Soc.* **2019**, *166* (15), C580–C588. <https://doi.org/10.1149/2.1021914JES/XML>.
- (31) Kanoufi, F. Electrochemistry and Optical Microscopy. *Encycl. Electrochem.* **2021**, 1–80. <https://doi.org/10.1002/9783527610426.BARD030108>.
- (32) Williams, G.; Kousis, C.; McMurray, N.; Keil, P. A Mechanistic Investigation of Corrosion-Driven Organic Coating Failure on Magnesium and Its Alloys. *npj Mater. Degrad.* **2019**, *3*, 41. <https://doi.org/10.1038/s41529-019-0103-4>.
- (33) Redor, S.; Godeffroy, L.; Rouse, G.; Abakumov, A. M.; Li, B.; Kanoufi, F.; Tarascon, J.-M. Electrochromic Corundum-like Compound Based on the Reversible (De)Insertion of Lithium:  $\text{Li}_2\text{Ni}_2\text{W}_2\text{O}_9$ . *J. Am. Chem. Soc.* **2023**, *145* (23), 12823–12836. <https://doi.org/10.1021/jacs.3c03631>.
- (34) Godeffroy, L.; Aguilar, I.; Médard, J.; Larcher, D.; Tarascon, J.-M.; Kanoufi, F. Decoupling the Dynamics of Zinc Hydroxide Sulfate Precipitation/Dissolution in Aqueous Zn–MnO<sub>2</sub> Batteries by Operando Optical Microscopy: A Missing Piece of the Mechanistic Puzzle. *Adv. Energy Mater.* **2022**, *12* (30), 2200722. <https://doi.org/10.1002/aenm.202200722>.
- (35) Godeffroy, L.; Lemineur, J.-F.; Shkirskiy, V.; Vieira, M. M.; Noël, J.-M.; Kanoufi, F. Bridging the Gap between Single Nanoparticle Imaging and Global Electrochemical Response by Correlative Microscopy Assisted By Machine Vision. *Small Methods* **2022**, *6* (9), 2200659. <https://doi.org/10.1002/SMTD.202200659>.
- (36) Li, R.; Makogon, A.; Galochkina, T.; Lemineur, J.-F.; Kanoufi, F.; Shkirskiy, V. Unsupervised Analysis of Optical Imaging Data for the Discovery of Reactivity Patterns in Metal Alloy. *Small Methods* **2023**, just accepted. <https://doi.org/10.1002/smt.202300214>.
- (37) Lemineur, J.-F.; Wang, H.; Wang, W.; Kanoufi, F. Emerging Optical Microscopy Techniques for Electrochemistry. *Annu. Rev. Anal. Chem.* **2022**, *15* (1), 57–82.

<https://doi.org/10.1146/annurev-anchem-061020-015943>.

- (38) Puigdomenech, I. Chemical Equilibrium Diagrams  
<https://sites.google.com/site/chemdiagr/home> (accessed Jul 6, 2023).
- (39) Majzlan, J.; Grevel, K.-D.; Navrotsky, A. Thermodynamics of Fe Oxides: Part II. Enthalpies of Formation and Relative Stability of Goethite ( $\alpha$ -FeOOH), Lepidocrocite ( $\gamma$ -FeOOH), and Maghemite ( $\gamma$ -Fe<sub>2</sub>O<sub>3</sub>). *Am. Mineral.* **2003**, *88*, 855–859.  
<https://doi.org/https://doi.org/10.2138/am-2003-5-614>.
- (40) Nasrazadani, S.; Raman, A. Formation and Transformation of Magnetite (Fe<sub>3</sub>O<sub>4</sub>) on Steel Surfaces under Continuous and Cyclic Water Fog Testing. *Corrosion* **1993**, *49* (4), 294–300.  
<https://doi.org/10.5006/1.3316052>.
- (41) Bernabale, M.; Cognigni, F.; Nigro, L.; Rossi, M.; de Caro, T.; De Vito, C. A Comprehensive Strategy for Exploring Corrosion in Iron-Based Artefacts through Advanced Multiscale X-Ray Microscopy. *Sci. Rep.* **2022**, *12* (1), 1–9. <https://doi.org/10.1038/s41598-022-10151-w>.
- (42) <https://refractiveindex.info/>.
- (43) Al-Kuhaili, M. F.; Saleem, M.; Durrani, S. M. A. Optical Properties of Iron Oxide ( $\alpha$ -Fe<sub>2</sub>O<sub>3</sub>) Thin Films Deposited by the Reactive Evaporation of Iron. *J. Alloys Compd.* **2012**, *521*, 178–182. <https://doi.org/10.1016/j.jallcom.2012.01.115>.
- (44) Batsanov, S. S.; Ruchkin, E. D.; Poroshina, I. A. *Refractive Indices of Solids (SpringerBriefs in Applied Sciences and Technology)*, 1st Editio.; Springer, 2016.
- (45) Go, S.; Lyapustin, A.; Schuster, G. L.; Choi, M.; Ginoux, P.; Chin, M.; Kalashnikova, O.; Dubovik, O.; Kim, J.; Da Silva, A.; Holben, B.; Reid, J. S. Inferring Iron-Oxide Species Content in Atmospheric Mineral Dust from DSCOVR EPIC Observations. *Atmos. Chem. Phys.* **2022**, *22* (2), 1395–1423. <https://doi.org/10.5194/acp-22-1395-2022>.
- (46) Chowdhury, D. R.; Spiccia, L.; Amritphale, S. S.; Paul, A.; Singh, A. A Robust Iron Oxyhydroxide Water Oxidation Catalyst Operating under near Neutral and Alkaline Conditions. *J. Mater. Chem. A* **2016**, *4* (10), 3655–3660. <https://doi.org/10.1039/c6ta00313c>.
- (47) Beverskog, B.; Puigdomenech, I. Revised Diagrams for Iron At 25-300 ° C. *Corros. Sci.* **1996**, *38* (12), 2121–2135.
- (48) Chase, M. W. J. Phys. Chem. Ref. Data, Monograph 9. In *NIST-JANAF Thermochemical Tables, Fourth Edition*; 1998; pp 1–1951.
- (49) Song, Y.; Jiang, G.; Chen, Y.; Zhao, P.; Tian, Y. Effects of Chloride Ions on Corrosion of Ductile Iron and Carbon Steel in Soil Environments. *Sci. Rep.* **2017**, *7* (1).

<https://doi.org/10.1038/s41598-017-07245-1>.

- (50) Critelli, R. A. J.; Bertotti, M.; Torresi, R. M. Probe Effects on Concentration Profiles in the Diffusion Layer: Computational Modeling and near-Surface PH Measurements Using Microelectrodes. *Electrochim. Acta* **2018**, *292*, 511–521. <https://doi.org/10.1016/j.electacta.2018.09.157>.
- (51) Klymenko, O. V.; Svir, I.; Amatore, C. New Theoretical Insights into the Competitive Roles of Electron Transfers Involving Adsorbed and Homogeneous Phases. *J. Electroanal. Chem.* **2013**, *688*, 320–327. <https://doi.org/10.1016/j.jelechem.2012.07.022>.
- (52) Amatore, C.; Szunerits, S.; Thouin, L.; Warkocz, J. S. The Real Meaning of Nernst's Steady Diffusion Layer Concept under Non-Forced Hydrodynamic Conditions. A Simple Model Based on Levich's Seminal View of Convection. *J. Electroanal. Chem.* **2001**, *500* (1–2), 62–70. [https://doi.org/10.1016/S0022-0728\(00\)00378-8](https://doi.org/10.1016/S0022-0728(00)00378-8).
- (53) Frankel, G. S. Pitting Corrosion of Metals: A Review of the Critical Factors. *J. Electrochem. Soc.* **1998**, *145* (6), 2186–2198.
- (54) Munteanu, S.; Roger, J. P.; Fedala, Y.; Amiot, F.; Combellas, C.; Tessier, G.; Kanoufi, F. Mapping Fluxes of Radicals from the Combination of Electrochemical Activation and Optical Microscopy. *Faraday Discuss.* **2013**, *164*, 241–258. <https://doi.org/10.1039/c3fd00024a>.
- (55) Jorcin, J.-B.; Blanc, C.; Pébère, N.; Tribollet, B.; Vivier, V. Galvanic Coupling Between Pure Copper and Pure Aluminum. *J. Electrochem. Soc.* **2008**, *155* (1), C46–C51. <https://doi.org/10.1149/1.2803506>.
- (56) Snihirova, D.; Höche, D.; Lamaka, S.; Mir, Z.; Hack, T.; Zheludkevich, M. L. Galvanic Corrosion of Ti6Al4V -AA2024 Joints in Aircraft Environment: Modelling and Experimental Validation. *Corros. Sci.* **2019**, *157*, 70–78. <https://doi.org/10.1016/j.corsci.2019.04.036>.
- (57) Park, H.; Takmakov, P.; Lee, H. Electrochemical Evaluations of Fractal Microelectrodes for Energy Efficient Neurostimulation. *Sci. Rep.* **2018**, *8* (1), 1–11. <https://doi.org/10.1038/s41598-018-22545-w>.